[5]A. Baldereschi, Bull. Am. Phys. Soc. **17**, 237 (1972); D. J. Chadi and M. L. Cohen, Phys. Rev. B 7, 692 (1973).
[6]J. Callaway, *Energy Band Theory* (Academic, New York, 1964), p. 56 and also Appendix 1.
[7]J. P. Walter and M. L. Cohen, Phys. Rev. B **4**, 1877 (1971).
[8]L. Kleinman and J. C. Phillips, Phys. Rev. **116**, 880 (1959).

PHYSICAL REVIEW B VOLUME 7, NUMBER 12 15 JUNE 1973

Cyclotron Resonance and the Cohen Nonellipsoidal Nonparabolic Model for Bismuth. III. Experimental Results*

Robert J. Dinger† and A. W. Lawson
Department of Physics, University of California, Riverside, California 92502
(Received 11 April 1972; revised manuscript received 7 December 1972)

Complete measurements of the anisotropy of the central-orbit cyclotron effective masses by Azbel'–Kaner cyclotron resonance have been taken at a frequency of 24.03 GHz and a temperature of 1.15 °K for the magnetic field in the three crystallographic planes of Bi. Deviations of up to 10% from ellipsoidal behavior were observed for the electron-effective-mass anisotropies. Except in one instance, the various effective-mass anisotropies give a good fit to the Cohen nonellipsoidal nonparabolic (NENP) model and the fit is clearly superior to the Lax ellipsoidal nonparabolic model fit. The ratio of the Fermi energy to the L-point band-gap energy, E_F/E_g, was determined from fitting the NENP model and found to be 1.5 ± 0.4, in good agreement with other measurements. The fit to the NENP model also indicated that m_2/m_2' is approximately 1, implying that the L-point valence and conduction bands have identical parameters. The cyclotron effective masses agree within 3% with the values obtained by Edel'man and Khaikin, and disagree by as much as 30% with the values obtained by Kao. Quantum oscillations of the microwave surface impedance similar in nature to de Haas–Schubnikov oscillations have also been observed, but periods arising from the large cross-sectional areas could not be detected and no conclusions regarding the NENP model could be made. Magnetoplasma oscillations due to standing Alfvén waves have also been observed. The mass-density values derived from these measurements agree with the values obtained by other investigators. However, the carrier concentration derived from the Alfvén-wave periods differs by nearly 12% with the value derived from the Azbel'–Kaner cyclotron-resonance measurements. This difference may be due to nonellipsoidal effects.

I. INTRODUCTION

In spite of a wealth of experimental measurements on the electron Fermi surface of Bi, the exact shape of the surface is still somewhat uncertain. Two recent papers, for example, are at odds with each other. Herrmann *et al.*,[1] from rf-size-effect measurements, obtain data which supports the Cohen nonellipsoidal nonparabolic (NENP) model[2] of the electron Fermi surface, whereas the magneto-optical results of Maltz and Dresselhaus[3] support the Lax ellipsoidal nonparabolic (ENP) model.[4] In two earlier papers[5,6] (hereafter referred to as I and II, respectively), we analyzed the Azbel'–Kaner cyclotron-resonance (AKCR) data of Edel'man and Khaikin[7] (hereafter, EK) and Kao[8] and, with a few exceptions, found reasonable agreement with the NENP model. The various discrepancies between experiments and the Fermi-surface models for Bi have been reviewed in I and II.

In hopes of clarifying the situation, we undertook further measurements of cyclotron resonance in Bi. At the outset, we were motivated by our ability to observe quantum oscillations (QO) of the microwave surface impedance similar in origin to de Haas–Shubnikov oscillations and magnetoplasma oscillations of the Alfvén-wave type, in addition to cyclotron resonance. All three phenomena were observed during the same liquid-helium run, with no basic change in measurement method required, a circumstance which had the potential to reveal fine deviations of the Fermi surface from ellipsoidality. For example, by forming the ratio of the cyclotron effective mass m^* and the extremal cross-sectional area A_{ext} (the parameter obtained from the QO), the deviations expected for the NENP model are about 20% instead of the 10% or so expected in either m^* or A_{ext} alone. The fact that the phenomena were observable simultaneously meant that errors due to sample handling, misalignment, temperature variations, and the like would not be present, as they might be if data from different investigators were combined.

Unfortunately, in spite of the fact that QO were observable over a large angular range, it turned out that at the crucial angles where the ratio might be expected to show up the deviations, the QO disappeared, apparently because of a lack of sufficient resolution in our apparatus. Hence, our original motivation for undertaking the present set

of measurements did not completely work out. However, by holding the AKCR errors to a maximum of about 4% and more typically 2%, a consistent deviation of the m^* anisotropy curves from the ellipsoidal model was observed. Moreover, a fairly good fit to the NENP model was obtained in most cases. In this paper, we report the AKCR results in detail, and summarize the QO and Alfvén-wave results.

II. THEORETICAL CONSIDERATIONS

A. Brief Review of Oscillatory-Surface-Impedance Phenomena in Bi

1. Azbel'-Kaner Cyclotron Resonance

Since Azbel' and Kaner's original paper[9] predicting the effect, AKCR has been observed in many metals. The conditions for observing the effect as treated by them require that r, the radius of a cyclotron orbit, and l, the mean free path, be much larger than the skin depth δ. Then, when the external magnetic field $\vec{H}$ is applied parallel to the surface of the sample, the spiraling carriers interact repeatedly with the microwave electric field $\vec{E}_{mw}$ in the skin depth. At certain values of the magnetic field H_N, the orbital cyclotron frequency will be an integral multiple of the frequency of the microwave electric field, and resonant absorption of energy by the carriers will occur. The values of H_N are given by

$$\frac{1}{H_N} = \frac{Ne}{\omega_{mw} m^* c}, \tag{1}$$

where ω_{mw} is the microwave frequency (in radians) and m^* is the cyclotron effective mass. Hence, AKCR allows one to measure the value of m^* by using Eq. (1).

The AKCR effect is strongest when $\vec{E}_{mw}$ and $\vec{H}$ are perpendicular to each other. For this orientation, the electron orbits whose cyclotron effective mass enters into Eq. (4) are extremal orbits, i.e., orbits whose cyclotron effective mass satisfies $\partial m^*/\partial k_H = 0$, where $k_H = \vec{k} \cdot \vec{H}/|\vec{H}|$. These orbits, in the case of Bi and in general in the case of any nonreentrant Fermi surface with a center of inversion, lie in a plane which contains the center of inversion and are called central orbits (CO). The CO cyclotron effective mass can be related to the geometry of the Fermi surface by the equation

$$m^*_{CO} = \frac{1}{2\pi} \left. \frac{\partial A_{ext}}{\partial E} \right|_{E=E_F}. \tag{2}$$

In this equation, A_{ext} is the extremal cross-sectional area of the Fermi surface perpendicular to $\vec{H}$. We are able to use the definition $\partial A_{ext}/\partial E$ in Eq. (2) rather than the more general definition $(\partial A/\partial E)_{ext}$ (where A is not necessarily extremal) because of the assumption of a centrosymmetric nonreentrant Fermi surface. All of the AKCR data reported here are CO data.

The two conditions for observing AKCR mentioned above ($r, l \gg \delta$) are always true (for good samples) for pure-metal single crystals at liquid-helium temperatures, but in the case of Bi must be examined more closely. Because of the lower carrier concentration in Bi, $\vec{E}_{mw}$ penetrates further into the crystal than in the case of metals and the condition that $r \gg \delta$ may not always be satisfied in Bi. In fact, a simple calculation shows that $r \simeq \delta$ for fields on the order of 500 G. The breakdown of the condition $r \gg \delta$ shows up in the data in the form of a distortion of the line shape from the form predicted by the theory and in a shift of the peak position from the value predicted by Eq. (1). In the present work, the cyclotron-effective-mass values were calculated from those peaks of a series which occurred below 200 G, where possible. We might add that frequently peaks of a series which occurred above 200 G, including fundamentals above 1000 G, fitted Eq. (1) quite well, even though $r \lesssim \delta$. Kao[8] has given a qualitative explanation of why AKCR is apparently still observable even when $r \lesssim \delta$.

2. Quantum Oscillations

The QO, when observable, commenced near 1000 G and continued to the highest fields used (15 kG). The oscillations were analyzed on the assumption that they are de Haas–Shubnikov-type oscillations, which result from the passage of Landau levels through the extremal areas of the Fermi surface. The period Δ of the oscillations in $1/H$ is related to the geometry of the Fermi surface by the relation due to Onsager,[10]

$$A_{ext} = 2\pi e\hbar/c\Delta, \tag{3}$$

where as before A_{ext} is the extremal cross-sectional area of the Fermi surface perpendicular to $\vec{H}$. Area anisotropies consistent with the AKCR results were obtained when the oscillations were analyzed in this manner, confirming that they are de Haas–Shubnikov-type oscillations.

3. Standing Alfven Waves

Treating the electron and hole charge carriers in pure Bi as a cold, compensated solid-state plasma with an isotropic relaxation time, Issacson and Williams[11] show that a dispersion relation of the form

$$k^2 = \frac{4\pi m_0 \omega_{mw}^2}{H^2} f(n_+, n_-, m_i, M_i) \tag{4}$$

results. The quantity k is the wave number of the magnetoplasma wave, m_0 is the free-electron mass, and f is the so-called mass density, a complicated

function of the hole and electron concentrations, the elements of the hole and electron effective-mass tensors, and the orientation of $\vec{H}$ and $\vec{E}_{mw}$. The inverse field dependence of wave number is characteristic of Alfvén-type waves. Because the Alfvén wavelength is a function of magnetic field, at certain values of the magnetic field H_N, an integral number of half-wavelengths, N, will be contained in the sample thickness. When this happens, a minimum occurs in the microwave surface impedance. Magnetoplasma waves in the pure Alfvén mode were observed in the two samples whose opposite faces were sufficiently parallel and smooth to show this Fabry–Perot-type resonance.

The relationship between H_N and N for a sample of thickness d is easily found to be

$$(\omega_{mw}/H_N)(4\pi m_0 f)^{1/2} d = N\pi \ . \tag{5}$$

Assigning the lowest value of N to the peak at the highest field and numbering the peaks in order, it is seen by Eq. (5) that a plot of $1/H_N$ versus N is a straight line whose slope is proportional to f.

Equation (4) is actually only approximately correct, and its derivation neglects such factors as the magnetic field dependence of the Fermi energy.[12] An essentially linear plot of N versus $1/H_N$ results only if the values of H_N used are much less than the value of the magnetic field which forces the $n=1$ Landau level through the extremal orbit on the Fermi surface. For Bi, this value of H depends on orientation and has a minimum value of about 13 kG. In all cases, the value of f was computed from the low-field, linear part of the N-versus-$1/H_N$ plot.

B. Anisotropy Equations

The NENP dispersion relation, given in the Appendix, in its most general form allows the conduction and valence bands to have different values for m_2. In I we derived the NENP cyclotron-effective-mass anisotropy assuming that $m_2 = m_2'$ (m_2' is the valence-band parameter). In order to obtain the most information from the experimental data, for this work we have derived the appropriate equations for the case $m_2 \neq m_2'$. The procedure is identical to the procedure used in I, but the algebra involved is considerably longer and more tedious. In the Appendix we have listed the resulting equation for the anisotropy.

III. EXPERIMENTAL ASPECTS

The samples used in this work are the same as those used by Everett[13] in an earlier perpendicular-field cyclotron-resonance study in 1961. As described in Ref. 13, the samples were made by a Bridgman technique and the surface produced by spark cutting, followed by chemically lapping the crystals on a cloth saturated with the standard polishing solution for pure Bi. After their use in 1961, the samples were untouched until the present investigation was begun in 1969. Over the intervening eight years, the samples presumably were annealing; the ideal annealing temperature of pure Bi is roughly of the order of room temperature. We attribute our ability to observe as many as 21 AKCR subharmonics at least in part to this long-term annealing process. The inferior binary-plane samples had to be cut and repolished for the work reported here because it exceeded the inside dimensions of the liquid-helium Dewar. The resulting surface obtained by the repolishing was not as flat as the original surface. All three samples were in the form of slabs with accurately parallel sides and were about 5 mm thick.

The measurement techniques used in this experiment were fairly standard. An end-mounted reflection-type cavity was employed in which the sample formed one end of the cavity. The sample normal was vertical and parallel to the direction of propagation. A small 40-Hz modulation field was added on top of the slowly varying applied field and synchronous detection used at 40 Hz. A $1/H$ sweep was used in conjunction with a proportional modulation-width controller in order to sweep large field intervals, while not running the risk of over- or undermodulation. The modulation-width controller varied the modulation-signal amplitude, so that the ratio of modulation amplitude to applied field was essentially constant.

The klystron source was tuned to 24.0 GHz and reflected power from the cavity monitored with a circulator. All measurements were made at 1.15 °K. The magnetic field was generated by an iron-core magnet capable of producing a 23.5-kG field in a 2-in. gap. The magnetic field was measured by a Rawson–Lush rotating-coil gaussmeter with a stated accuracy of at least 0.01%. The calibration of the gaussmeter was checked with a Varian NMR probe. The magnet rested on a rotating platform, so that the field could be rotated 360° in a horizontal plane. The magnetic field direction was parallel to the surface of the sample to better than 1°.[14]

IV. EXPERIMENTAL RESULTS

A. AKCR Results

The cyclotron effective masses were obtained by least-squares fitting of a curve to the variables N, the peak index, and $1/H_N$, the peak-field-value reciprocal. Cooper and Lawson[15] have described at length the problems encountered using least-squares-fitting techniques when one of the variables takes on only integer values.

The uncertainties in the determination of the cyclotron effective mass arise from difficulties associated with accurately locating the H_N, such

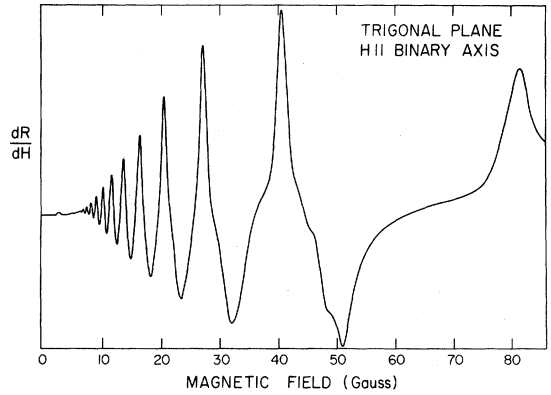

FIG. 1. Azbel'–Kaner cyclotron-resonance trace for the magnetic field in the trigonal plane and parallel to the binary axis

as interfering mass branches and broadened peaks in low-$\omega\tau$ samples, and from shifts in the true location of H_N due to experimental errors such as nonlinearities in the magnetic field sweep. For the bisectrix and trigonal samples, the cumulative effect of these errors was usually about 1% or less and was smallest for $\vec{H}$ in the small-mass directions. Near the large-mass directions, these errors were occasionally 3%, but 2% was a more typical figure. Generally speaking, we can say that the relative error in m^* from one point to the next is no greater than about 3% for the bisectrix and trigonal samples. For the binary sample, however, this relative error was somewhat larger because of the lower value of $\omega\tau$. Occasional uncertainties of 6% were encountered, but 4% and less were more typical.

1. Trigonal (XY) Plane

In the trigonal plane, the most complete set of AKCR data of any plane was taken. Figure 1 shows an AKCR trace for $\vec{H}$ parallel to the binary axis and $\vec{E}_{mw} \perp \vec{H}$. At least 20 peaks could be resolved in the low-field $m_{II}^* - m_{III}^*$ branch, although in Fig. 1 only about 15 can be seen because of the low gain required to keep the low-order subharmonics from saturating the electronics. The number of subharmonic peaks which can be resolved for a particular mass branch varied markedly with the orientation of $\vec{H}$. As $\vec{H}$ is rotated from an orientation parallel to the small-effective-mass direction ($\vec{H} \parallel \vec{p}_1$) to the large-effective-mass direction ($\vec{H} \perp \vec{p}_1$), the number of observable subharmonics decreases from 20 to about nine. This decrease is attributable to the anisotropy of the electron relaxation time. [16,17]

The variation of the measured CO mass with the orientation of $\vec{H}$ is given in Fig. 2 for the electrons, along with the curves computed for the ENP and NENP models. Figure 3 is a polar plot of the small effective masses in the trigonal plane. For all the points shown on Fig. 3, the ENP and NENP curves coincide.

The differences between the models occur near the orientations of $\vec{H}$ where the cyclotron effective mass is largest, a statement true in general for every plane. In Fig. 2, the curve computed for the NENP model for $r = 1.0$ and $\lambda = 2.0$ is observed to fit the experimental points quite well, and the fit to the NENP model is clearly superior to the fit to the ENP model. For any r there is always a value of λ giving a curve which fits the data as

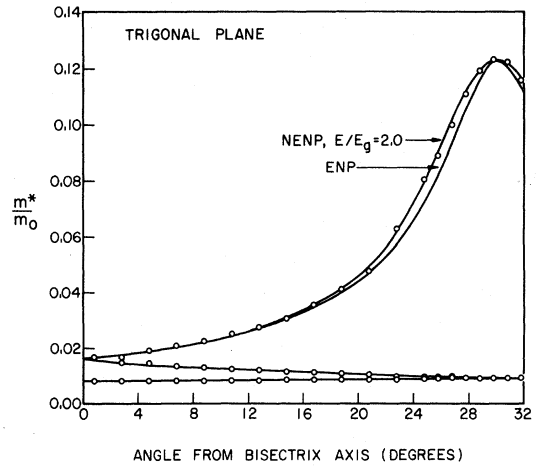

FIG. 2. Cyclotron effective masses observed in the trigonal plane compared with curves generated from the ENP and NENP models.

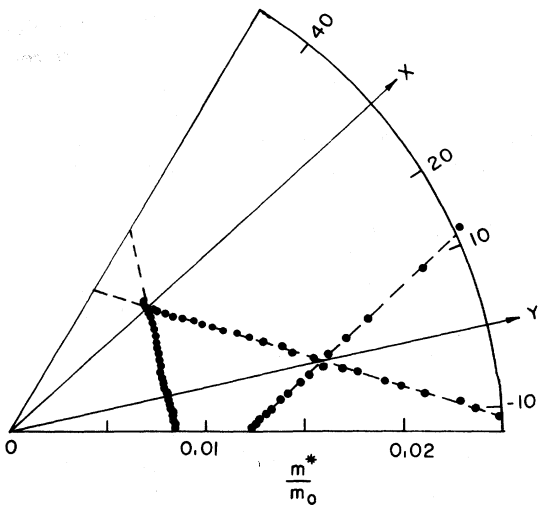

FIG. 3. Polar plot of small electron cyclotron effective masses observed in the trigonal plane of Bi. The curves are generated from both the ENP and NENP models, which coincide for the points shown here.

TABLE I. Band-structure parameters reported in the literature for Bi.

Investigator	Ref.	E_F (meV)	E_g (meV)	E_F/E_g	r
Jain	18	17.7	7	2.5	
Brown *et al.*	19	25	15	1.7	
Weiner	20	22	46	0.5	
Engeler	21	22[a]	24	0.9	
Hebel and Wolff	22	27	14	1.9	
Smith *et al.*	23	27.6	15[b]	1.8	
Brown and Silverman	24	21	24	0.9	
Esaki and Stiles	25	15	20	0.75	
Strom *et al.*	26	29.2	12	2.4	
Brandt *et al.*	27	27	20	1.3	
EK[c]	7			1.7	
EK[d]	7			0.5	
Bate *et al.*	28				3
Antcliffe and Bate	29				~1
Ellet *et al.*	30				≫1

[a]Assumed value found in Ref. 20.
[b]Assumed value found in Ref. 19.
[c]As interpreted by Dinger and Lawson, Ref. 5.
[d]As interpreted by Dinger and Lawson, Ref. 6.

well as the choice $r = 1.0$, $\lambda = 2.0$. In other words, unfortunately, there is not a unique pair of values of r and λ which gives a best fit. Under these circumstances the best that can be done is to assume a value of one of the parameters and determine a value for the other parameter on the basis of the best fit to the experimental points. The values of λ and r determined by other investigators are given in Table I. From this table, it is obvious that the least information is known about r. In most electron Fermi-surface studies in Bi, r is assumed to be 1.0. However, the series of de Haas–Shubnikov experiments by Bate and his co-workers[28,29] and Ellet *et al.*[30] using Bi alloys in order to raise and lower the Fermi level have given direct information on the value of r. Unfortunately, these experiments have given inconsistent results, indicating either that $r \simeq 1$, $r \simeq 3$, or $r \gg 1$.

Values of λ have also varied considerably, but here there seems to be a general consensus that the value $\lambda = 1.7$ determined by several experiments is the best value. The only direct measurement of λ was in Ref. 25, using tunneling spectroscopy, and a value 0.75 was obtained. However, the interpretation of these tunneling measurements is not unambiguous, and there is some question about the validity of the 0.75 figure. Clouding the issue still further is the fact that in I and II, we found evidence for a value of $\lambda = 0.50$.

Under these circumstances we have chosen to begin by assuming a value of $r = 1.0$ and performing a least-squares fit to determine the best value of λ. If a totally unreasonable value of λ were to result, i.e., outside the range 0.5–1.7, then a new value of r would be assumed and the least-squares fit performed again. As it turns out, we have to go further than the first step. Assuming a value of $r = 1.0$ gives $\lambda = 1.44$, a quite reasonable value. A logical question to ask is what range of r results when λ is allowed to vary between 0.5 and 1.7. The answer can be found in Fig. 4. Values of r and λ which result in the best least-squares fit to the data points give the curve shown on the graph. The portion of the curve within the rectangle represents the most logical values of r and λ, based on $0.5 < \lambda < 1.7$. The point to notice is that the range of r within this rectangle is fairly small ($0.9 < r < 1.7$) and is near unity. In particular, a value of $r = 3$ (which is the value found by Bate *et al.*[28]) requires $\lambda = 0.20$, which is an entirely unreasonable value. Hence, from the trigonal-plane data we conclude that $r \simeq 1$, so that $m_2 \simeq m_2'$, as found by many other workers. For $r = 1.0$, in the trigonal plane, $\lambda = 1.44$.

2. *Bisectrix (XZ) Plane*

The bisectrix sample had the best $\omega\tau$ of any of the three samples; 22 peaks were observable for the most favorable orientation of $\vec{H}$, several more than were observable for the trigonal sample, and the signal-to-noise ratio was somewhat larger. The appearance of the bisectrix-sample field sweeps is essentially identical to the trigonal-sample sweeps.

The anisotropy results for the CO cyclotron effective mass in the bisectrix plane are shown in Fig. 5. The points for the m_{II}^* branch fit the NENP model quite well, and clearly fit it better than they fit the ENP model. For comparison with the trigonal plane (and in the next part, the binary plane), we have plotted the NENP curves

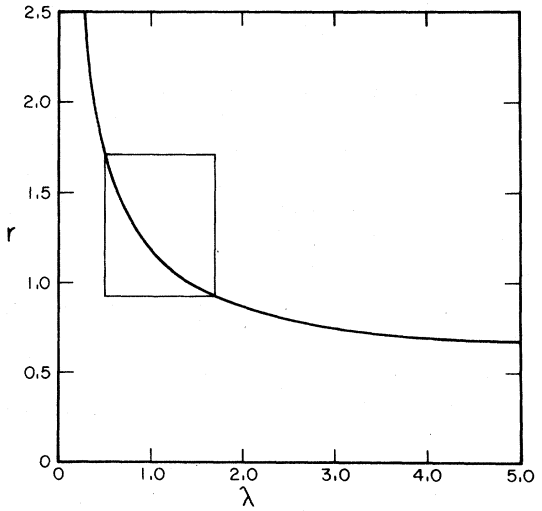

FIG. 4. Values for r and λ which give the best least-squares fit to the points near the effective-mass maximum in m_I^* in Fig. 2, as evaluated in the NENP model.

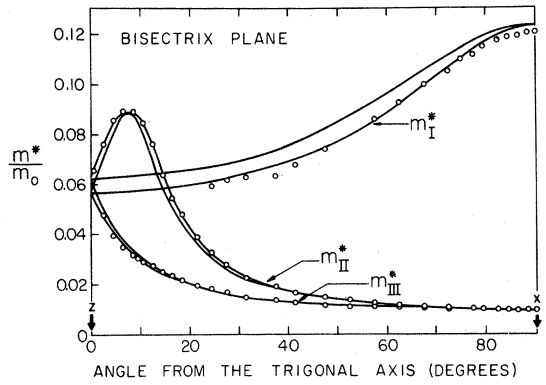

FIG. 5. Electron cyclotron effective masses observed in the bisectrix plane compared with curves generated from the ENP (lower curve in each case) and NENP (upper curve in each case) models.

for $\lambda = 2.0$, the same value used for all planes. A least-squares computer fit, however, gives a slightly different value. Again, we will initially choose $r = 1.0$ and compute a value for λ. The resulting least-squares-fit value is $\lambda = 2.23$ for $r = 1.0$. This value is somewhat larger than the value derived from the trigonal-plane data, but is not unreasonable. For the m^*_{II} branch in this plane, an analysis of the variation of r for changes in λ yields a graph essentially identical to Fig. 4, indicating that $r = 1$ and is most certainly not equal to 3.

For m^*_{III} in the region in which the data points are shown there is little difference between the two models. Near 8°, a slight mismatch between the data points and both the ENP and NENP models is evident. Although the disagreement involved is not much outside the experimental error, the pattern of disagreement suggests the presence of a slight crystal misalignment error.

Further evidence of a slight crystallographic misorientation is apparent in the m^*_I branch. This particular branch is very sensitive to misorientation errors. The rather large difference between the NENP model and the data points, and the probably fortuitous agreement with the ENP model, can be explained by a misorientation error between the surface normal and the true bisectrix axis of only 0.5°. A further difficulty is the similarity between the anisotropy of the m^*_I and hole branches in this plane (compare Figs. 5 and 6). Near the trigonal axis, the hole and electron masses are seen to be very nearly the same. As we move away from the trigonal axis towards the binary axis, the m^*_{II} and m^*_{III} branches depart from the hole-mass value and are easy to track. On the other hand, the m^*_I mass branch has an anisotropy much like the hole mass and the two masses are very close to each other over a considerable range of angles near the trigonal axis. The difficulty arises because the hole mass has a fairly low $\omega\tau$ as compared to the electron $\omega\tau$. Specifically, the holes have an $\omega\tau \simeq 10$ as opposed to ~18 for the electrons. Because the hole peaks are wider than the electron peaks, the electron peaks are sometimes completely obliterated, especially in the case of the high-order subharmonics. Hence, the large experimental errors and poor fit to either model for the m^*_I branch can be explained in this manner.

Returning to the hole cyclotron mass in Fig. 6, the curve there is elliptical, computed using the values of m^* for $\vec{H}$ parallel to the trigonal and binary axes as the extremal values for the ellipse. The derived values of the elements of the hole-effective-mass tensor are given below in Sec. V.

3. *Binary (YZ) Plane*

As mentioned in Sec. III, the binary sample has a surface which is probably not as flat as the other samples. The quality of the observed traces therefore suffers somewhat, as can be seen in Fig. 7, which is a trace taken for $\vec{H}$ parallel to the bisectrix axis. Whereas ~20 peaks were observable in the other two planes for this magnetic field orientation, only seven were observable in the binary plane. The principal effect of this low value of τ is to introduce a greater amount of scatter in the data points. As long as the slope method is used to compute the value of m^*, however, the derived values of m^* are essentially independent of τ.

Figure 8 is a plot of the data points near the trigonal axis, compared with the predictions of the two models. In the binary plane the m^*_{II} and m^*_{III} branches are degenerate; hence, there are only two electron branches shown in Fig. 8. As was

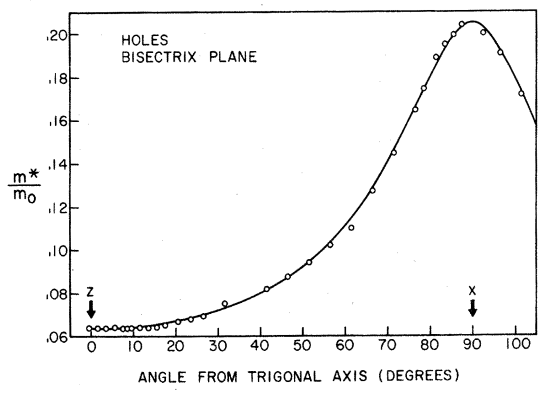

FIG. 6. Hole cyclotron effective masses observed in the bisectrix plane. The curve is an ellipse computed using the two extrema in the data points as end points of the ellipse.

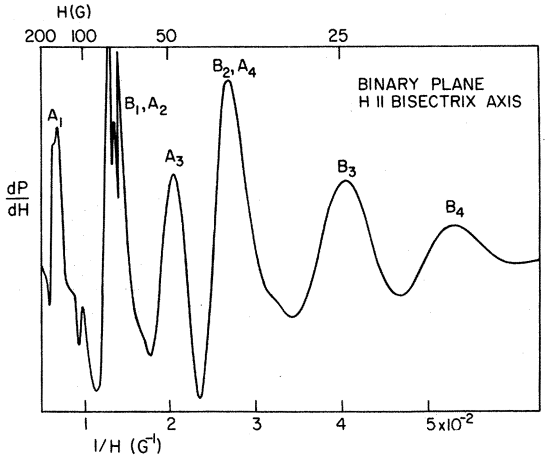

FIG. 7. AKCR trace for the magnetic field in the binary plane and parallel to the bisectrix axis. The *A* series of peaks are from electron orbits on quasiellipsoids II and III and the *B* series of peaks are from electron orbits on quasiellipsoid I.

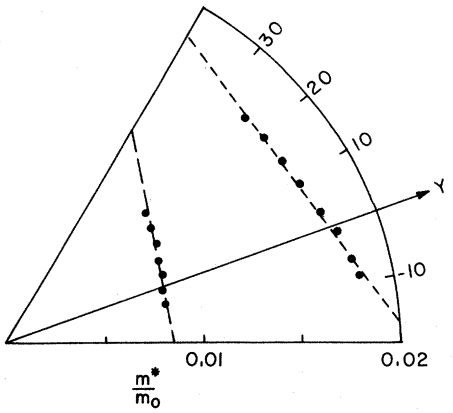

FIG. 9. Polar plot of electron cyclotron effective masses observed with the magnetic field in the binary plane in the vicinity of the bisectrix axis. The lines shown are for both the ENP and NENP models, which coincide at these angles.

the case in the trigonal and bisectrix planes, the data points fit the NENP model fairly well, and the fit is clearly better than the fit to the ENP model. As in the other two planes, we have plotted the NENP curve for $\lambda = 2.0$, although the least-squares fits give somewhat different values than 2.0. Part of the scatter in the m^*_{II}-m^*_{III} branch might be due to an incomplete degeneracy of the m^*_{II} and m^*_{III} masses because of a slight sample misorientation. A slight misorientation causes the peaks to be broader and would make the fields of the peaks harder to identify, leading to larger uncertainties in the masses.

The value for the tilt angle is most easily obtained from the binary-plane data: θ_t is the angular

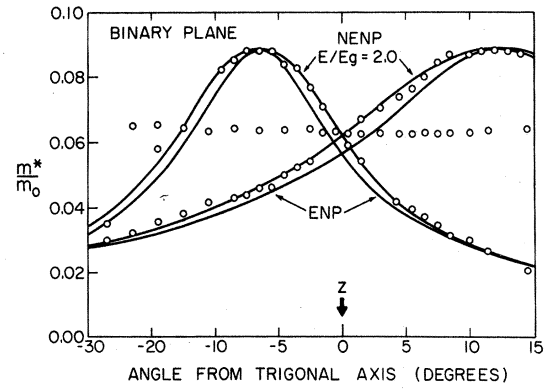

FIG. 8. Electron cyclotron effective masses observed in the binary plane in the vicinity of the trigonal axis compared with the curves generated from the ENP model and NENP model. The points with no curve are the hole cyclotron effective masses.

difference between the trigonal axis and the maximum in m^*_I. We measure this as $6.5° \pm 0.2°$. This value is also consistent with the data in the other two planes. Figure 9 is a polar plot of the data in the binary plane near the bisectrix axis.

The least-squares fit of the data to the NENP model was done assuming a value of $r = 1.0$. The resulting best value for λ is $\lambda = 1.13$ for m^*_I and $\lambda = 1.24$ for m^*_{II}-m^*_{III}. These again are quite reasonable values and do not justify any attempts to use a value of r different than 1.0.

The hole results are plotted in Fig. 10 for the binary plane. Good agreement is obtained with the ellipsoidal model.

B. Quantum-Oscillation Results

As discussed in the Introduction, the principal interest in the surface-impedance quantum oscillations is the information which can be obtained by combining the QO periods with the effective masses obtained from AKCR. The sought-for deviations from ellipsoidality occur near magnetic field directions where the cross-sectional areas of the Fermi surface are largest. By Eq. (3) this implies that the period becomes small. As it turned out, in our case the period became so small that the oscillations were unresolvable and vanished. We attribute the relatively low resolution to the nonoptimum geometry; i.e., the microwave surface impedance is apparently not the best quantity to measure in order to observe de Haas–Shubnikov oscillations. We note that Khaikin *et al.*[31] experienced the same difficulty in their microwave surface-impedance quantum-oscillation measurements on Bi.

Figure 11 is a typical field sweep for $\vec{H}$ in the binary plane near the trigonal axis. The short-

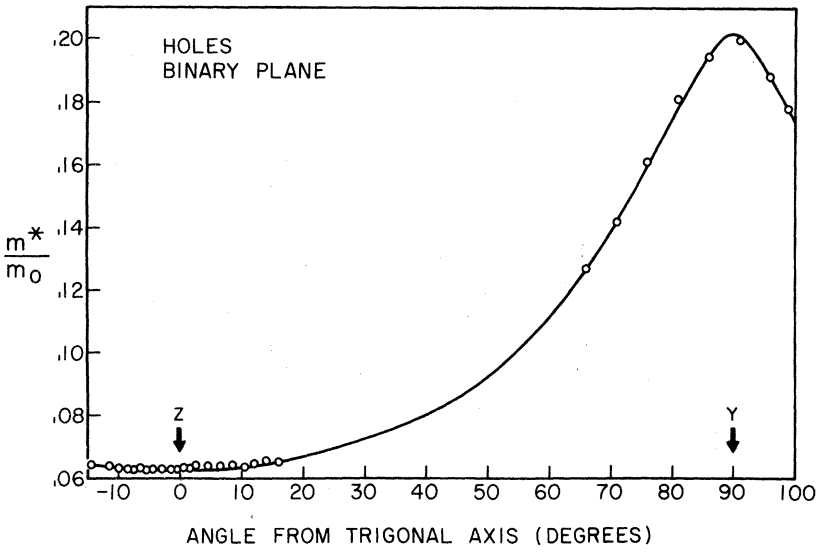

FIG. 10. Hole cyclotron effective masses observed in the binary plane. The curve is an ellipse computed using the two extrema in the data points as end points of the ellipse.

period oscillations are the standing Alfven waves, which will be discussed below. The oscillations of interest here form the envelope curve of the Alfven waves. The experimental error in determining the period from traces such as Fig. 11 is relatively large, on the order of 5% or more.

The anisotropy of the QO periods for $\vec{H}$ in the binary plane is shown in Fig. 12. The curve for only the ENP model have been shown because of a lack of data points of precision adequate to display any deviations from the ENP model. These deviations occur near the minima in the curves, where the square points are plotted in Fig. 12. From Fig. 12, it is apparent that near the trigonal axis, the hole periods dominate the observed traces and nearly obliterate the electron periods. This circumstance has manifested itself in every QO-type experiment in Bi. Bhargava[32] was the first to solve this problem by differentiating the signal and using a band-reject filter to delete the hole signal. Filtering techniques of this nature are clearly unusable here because of the Alfvén waves.

The anisotropy of Δ for $\vec{H}$ in the bisectrix plane is shown in Fig. 13, which displays the lack of data points for $\vec{H}$ near the trigonal axis. The scatter in the points results mainly from the relatively low number of peaks available to determine Δ (from two to five peaks in most cases) and from interference with AKCR peaks. We were unable to resolve more than one set of oscillations near

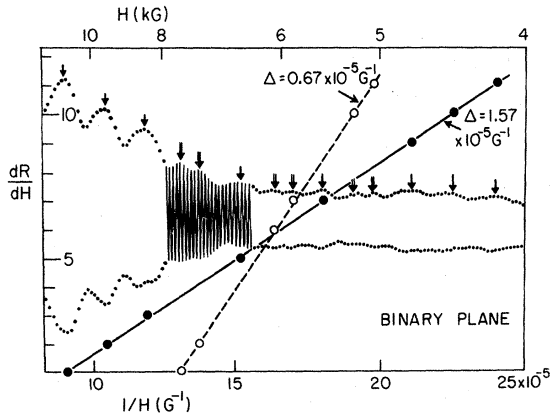

FIG. 11. Standing Alfvén waves and quantum oscillations observed in the binary plane with the magnetic field oriented 12° from the trigonal axis. The fast oscillations, which are the Alfvén waves, are shown in full only near 8 kG. The quantum oscillations form the envelope of the Alfvén waves, which are shown resolved into two separate oscillation periods by the arrows.

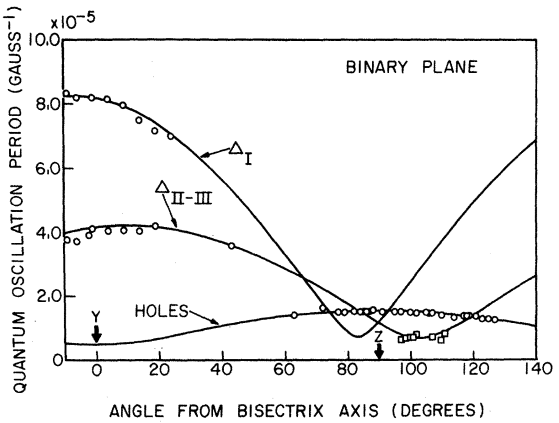

FIG. 12. Electron and hole quantum-oscillation periods observed for the magnetic field in the binary plane. The curves are computed from the ENP model.

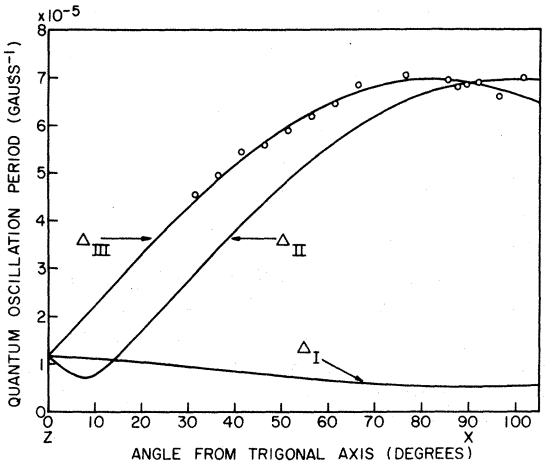

FIG. 13. Electron quantum-oscillation periods observed for the magnetic field in the bisectrix plane. The curves are computed from the ENP model.

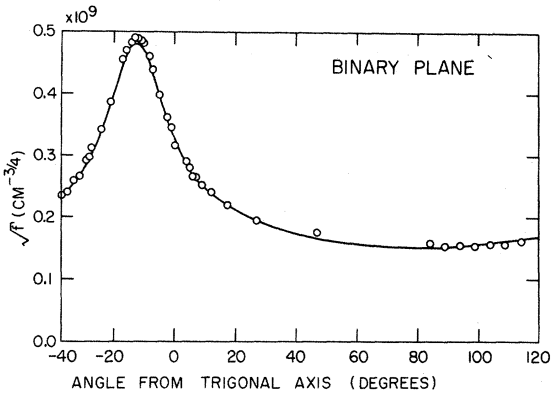

FIG. 15. Anisotropy of the Alfvén-wave mass density for the magnetic field in the binary plane. The curve is computed for an ellipsoidal model.

the binary axis, although two sets should exist. Again, however, we cannot make any comparison with the NENP model, since no data points could be taken in the angular region where the ENP and NENP models differ.

The poorest-quality QO were observed in the trigonal plane. Figure 14 displays the variation of Δ observed in this plane. There is a range of angles apparent where no QO of any kind were visible; the Alfvén-wave envelope was observed to flatten out in this region and had no discernible features. As was the case in the bisectrix plane, the data points measured in the trigonal plane occur at orientations of $\vec{H}$ at which the NENP and ENP models coincide.

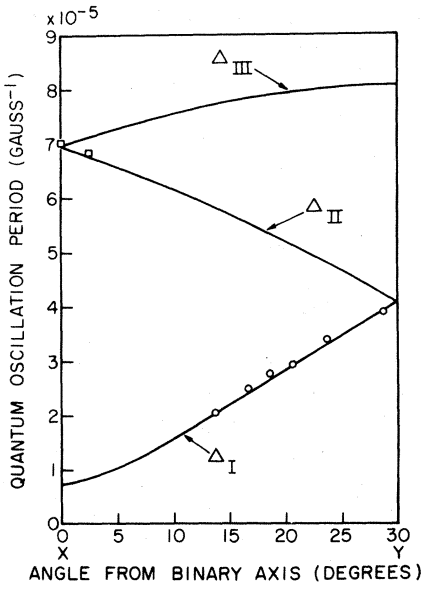

FIG. 14. Electron quantum-oscillation periods observed in the trigonal plane. The curves are calculated from the ENP model.

C. Alfvén-Wave Results

Standing Alfven waves were observable in the binary and trigonal planes.

A typical Alfven-wave trace has already been given in Fig. 11 for $\vec{H}$ in the binary plane. Figure 15 is a plot of the measured anisotropy of $\sqrt{f}$ in this plane. The curve in Fig. 15 was calculated from the ellipsoidal model by the procedure described by Isaacson and Williams.[11] For the case of $\vec{H}$ in the binary plane, the anisotropy equations have been given explicitly by Nagata and Kawamura.[33] The curve and data points agree well. The deviations near the maximum occur at an angle where the nonellipsoidal distortion of the electron Fermi surface is largest; it seems likely that the differences between theory and experiment are due to nonellipsoidal effects. The obvious method of verifying this possibility would be to derive the anisotropy equations for f in the NENP model. We have attempted this calculation, but thus far have been unsuccessful. The difficulty lies in the impossibility of writing the energy-momentum dispersion relation for the NENP model as quadratic form. This problem can be bypassed in the derivation of the extremal cross-sectional area and cyclotron effective masses by the technique used in I and II, specifically by employing explicit angle transformations rather than tensors in accounting for the rotation about the trigonal axis and the tilt of the electron quasiellipsoids. Such methods seem difficult or impossible to apply in the analysis of the Alfven waves.

At first glance, it may seem puzzling why one should not expect to see larger deviations between theory and experiment in Fig. 15, on the basis of

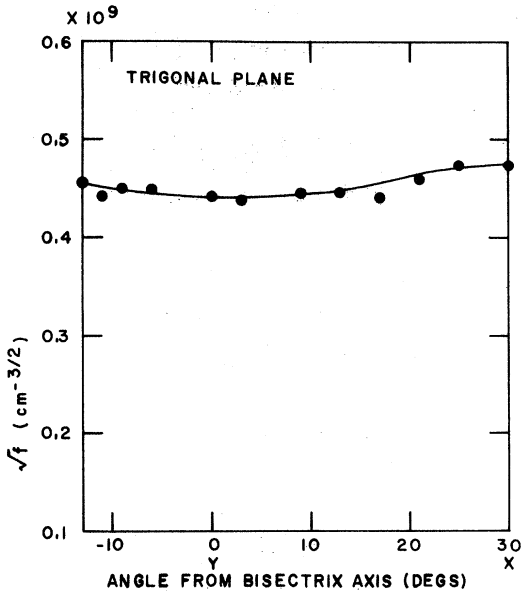

FIG. 16. Anisotropy of the Alfvén-wave mass density for the magnetic field in the trigonal plane. The curve is a hand-drawn curve through the points to indicate the trend.

the AKCR data. The reason is that f includes contributions from all sheets of the Fermi surface. Hence, at angles where a fairly large nonellipsoidal distortion is expected from one of the three electron quasiellipsoids, the other two quasiellipsoids, along with the hole surface, appear ellipsoidal and reduce any nonellipsoidal effects.

The measured anisotropy of the mass density in the trigonal plane is shown in Fig. 16. The curve is hand drawn through the points, and is not computed from any model. For purposes of detecting any deviations from ellipsoidality of the electron Fermi surface, it is pointless to compute a theoretical curve, as was done for the binary-plane data; in the trigonal plane the relatively large effective mass of the holes dominates the value of the mass density at all angles of the magnetic field. Since the hole effective mass is isotropic in the trigonal plane, there is very little variation in f, as is evident in Fig. 16.

V. DISCUSSION

The previous section presented the data from the three phenomena studied in this work. In this section we compare and combine these data to obtain values of the various parameters of the band structure and Fermi surface of Bi.

A. Value for E/E_g and Fermi Energies

Averaging the four values of λ found above gives $\lambda = 1.5 \pm 0.4$, which agrees with the generally accepted value of about 1.7 measured in several experiments. To derive a value for the electron Fermi energy, a value must be assumed for the gap energy. Fortunately, the value $E_g = 0.015 \pm 0.002$ eV has been found in several experiments (see Table I), so that this value can be assumed with confidence. This value gives $E_F = 0.023 \pm 0.007$ eV. We will use this number in further computations below.

A value for the hole Fermi energy E_F^h can be deduced by combining the AKCR and QO data for the holes for $\vec{H}$ parallel to the trigonal axis. Because the hole surface has a parabolic energy dispersion and is an ellipsoid of revolution about the trigonal axis, we have from Eq. (3) that the QO period for $\vec{H} \parallel \vec{Z}$ is

$$\Delta = e\hbar/cm^* E_F^h . \tag{6}$$

By solving Eq. (6) for E_F^h and inserting the values of m^* and Δ for $\vec{H} \parallel \vec{Z}$, a value for the hole Fermi energy can be calculated. Substituting $m^* = 0.064 m_0$ and $\Delta = 1.57 \times 10^{-5}$ G^{-1} gives

$$E_F^h = 0.0155 \pm 0.0005 \text{ eV} . \tag{7}$$

B. Effective-Mass-Tensor Components

The effective-mass-tensor components are most easily and directly obtained from the AKCR results. Given the values of the cyclotron effective masses for $\vec{H}$ along the three principal axis directions, m_i^* ($i = 1, 2, 3$ implies the p_i direction), then the elements of the effective-mass tensor at the Fermi level, m_i', are given by

$$m_i' = m_j^* m_k^* / m_i^* , \tag{8}$$

where the indices are permuted cyclically. In Table II we have summarized the effective masses measured in this work. Inserting the appropriate values given in Table II into Eq. (8) gives

$$\begin{aligned} m_1' &= 0.00597 m_0 , \\ m_2' &= 1.33 m_0 , \\ m_3' &= 0.0114 m_0 . \end{aligned} \tag{9}$$

These are the values which were used in the various equations for the effective-mass anisotropy in the ENP and NENP models. We should emphasize, however, that these values must first be reduced to the bottom of the band using the equations given in the Appendix of II before substitution into the anisotropy equations.

Table II also compares the cyclotron-effective-mass values with the values obtained from other cyclotron-resonance experiments in the literature. Of main interest is the comparison with the values of EK and Kao. As is obvious, the values compare much more favorably with the values of EK than with the values of Kao. The poor agreement between Kao's values and the values of EK

TABLE II. Comparison of the cyclotron effective masses observed in this experiment with the masses observed in other cyclotron-resonance experiments.

		Electrons					Holes		
		$\vec{H} \parallel \vec{X}$		$\vec{H} \parallel \vec{Y}$		$\vec{H} \parallel \vec{Z}$			
Investigator	Ref.	m_I^*	m_{II}^*, m_{III}^*	m_I^*	m_{II}^*, m_{III}^*	all	$\vec{H} \parallel \vec{X}$	$\vec{H} \parallel \vec{Y}$	$\vec{H} \parallel \vec{Z}$
Aubrey	34	0.119	0.009	0.0078	0.0156	0.06	0.15	0.15	0.04
Galt *et al.*	35	0.13	0.0105	0.0091	0.0180	0.08	0.25	0.25	0.068
Everett	13		0.0098	0.0077	0.0155	0.051			
Kao	8	0.14	0.0107	0.0091	0.0196	0.081	0.226	0.226	0.067
EK	7	0.120	0.0093	0.0081	0.0161	0.059	0.203	0.203	0.063
This work		0.123	0.0094	0.0083	0.0165	0.060	0.205	0.205	0.063

and this work can be attributed to the relatively low $\omega\tau$ of Kao's samples, which required him to compute the cyclotron effective masses from the position of the fundamental. As Kao acknowledges, this procedure can lead to a 20% or more error in the true effective mass. In passing, we might note that our verification of the results of EK is important because some investigators[36,37] have taken the effective-mass-tensor elements determined by Kao to be the better set of values.

If we had been successful in observing the Alfvén waves in all three planes, rather than just two, we could calculate a set of values for the elements of the effective-mass tensor following the procedure of Isaacson and Williams.[12] Instead, below we shall use the values of the effective-mass-tensor components obtained from AKCR in the equations of Isaacson and Williams to obtain a value for the hole and electron concentrations.

C. Quantum-Oscillation Periods

Table III summarizes the QO periods measured in this work and compares them with some of the de Haas–van Alphen and de Haas–Shubnikov periods reported in the literature for pure Bi. The agreement is good, confirming that the observed oscillations result from the successive depopulation of Landau levels at the Fermi level.

D. Carrier Concentrations

The values of the carrier concentrations $n_\pm$ are related to the Fermi surface by

$$n_\pm = 2V_\pm/h^3 , \tag{10}$$

where $V_\pm$ is the total volume of the hole Fermi surface (for V_+) or the electron Fermi surface (for V_-). We consider the electron concentration first. For the NENP model the volume of the Fermi surface is easily found to be

$$V_{\mathrm{NENP}} = 8\pi (2m_1 m_2 m_3)^{1/2} E_F^{3/2} (1 + \tfrac{6}{5}\lambda). \tag{11}$$

Using $E_F = 0.023$ eV as found above and the values of the m_i' as given in Eq. (9) (after reducing them to the bottom of the band to get the m_i) results in

$$n_-^{\mathrm{NENP}} = 2.73\times10^{17}\ \mathrm{cm}^{-3} . \tag{12}$$

For the ENP model, the volume of the electron Fermi surface is given by

$$V_{\mathrm{ENP}} = 8\pi (2m_1 m_2 m_3)^{1/2} E_F^{3/2} (1+\lambda)^{3/2} . \tag{13}$$

Substituting into this equation, we obtain

$$n_-^{\mathrm{ENP}} = 2.19\times10^{17}\ \mathrm{cm}^{-3} . \tag{14}$$

The hole Fermi-surface volume is given by

$$V_+ = \tfrac{8}{3}\pi M_1 (2M_3)^{1/2} (E_F^h)^{3/2} , \tag{15}$$

where E_F^h is the hole Fermi energy. The values of M_1 and M_3 have been computed previously [Eq. (10)] and a value for E_F^h was found in Eq. (7) above. Substituting these values into Eq. (15) gives

$$n = 2.84\times10^{17}\ \mathrm{cm}^{-3} . \tag{16}$$

This value agrees to 4% with n_-^{NENP}, which is within the experimental errors. The agreement is to 20% with n_-^{ENP}. We feel that the superior agreement between n_+ and n_-^{NENP} argues in favor of a nonellipsoidal electron Fermi surface for Bi.

We can obtain another value for the electron and hole concentrations by combining the AKCR-derived effective-mass-tensor components and the Alfvén-waves results. As discussed in Sec. II, the Alfvén-wave period in inverse field, $\Delta(1/H)$, can be related to the mass density f. The quantity f in turn is a function of the effective-mass-tensor components, the orientation of the external mag-

TABLE III. Comparison of quantum-oscillation periods (in units of $10^{-5}\,\mathrm{G}^{-1}$) measured in this work with values reported in the literature.

		Electrons			Holes
Investigator	Ref.	$\vec{H} \parallel \vec{X}$	$\vec{H} \parallel \vec{Y}$		$\vec{H} \parallel \vec{Z}$
Brandt	38		4.3	8.2	1.56
Kunzler *et al.*	39	7.1	4.1	8.2	
Eckstein and Ketterson	40	7.6	4.5	8.9	1.6
Bhargava	32	7.20	4.17	8.30	1.575
Brown	41	7.03	4.07	8.15	1.57
This work		7.0	4.05	8.2	1.56

netic field, and the electron and hole concentrations. For $\vec{H}$ and the microwave electric field oriented along crystallographic axes, the expressions for f reduce to a tractable form. The appropriate equations are given in Ref. 11, where Isaacson and Williams used them to derive values of the hole and electron concentrations and the elements of the effective-mass tensor. Since we have values of the effective-mass-tensor elements from AKCR, we shall use the appropriate equations in Ref. 11 as four equations to determine n_+ and n_- by a least-squares fit. Substituting the values of the m_i and M_i, we obtain

$$n_- = 3.19 \pm 0.09 \times 10^{17}\ \text{cm}^{-3}$$

and (17)

$$n_+ = 3.09 \pm 0.09 \times 10^{17}\ \text{cm}^{-3}\ .$$

The source of the approximately 12% difference between the concentration values derived from the AKCR results and the Alfvén-wave results is somewhat difficult to assess. Most of the difference is probably attributable to the assumption of an ellipsoidal Fermi surface in the derivation of the equations in Ref. 11. We have attempted to derive the analogous equations starting from the NENP dispersion relation, but thus far have been unsuccessful.

VI. SUMMARY AND CONCLUSIONS

Complete measurements of the central-orbit cyclotron effective masses by Azbel'-Kaner cyclotron resonances were taken for the magnetic field in the three crystallographic planes of pure Bi. Quantum oscillations of the microwave surface impedance were observed in all three planes, but oscillations for $\vec{H}$ oriented normal to the large cross-sectional areas of the electron Fermi surface could not be detected, except in one case. Standing Alfvén waves were observed for the magnetic field in the binary and trigonal planes.

The main purpose of this experiment was to determine as accurately as possible the shape of the electron Fermi surface. Errors in the cyclotron-resonance portion of this work could be held to 4% or less and this uncertainty was sufficiently low to show that the electron Fermi surface is distorted by about 10% from an ellipsoid. Furthermore, the manner in which the surface is distorted seems to be predicted fairly accurately by the Cohen band-structure model.

The implications of the value of $m_2/m_2' \sim 1$ found here are interesting. First, we emphasize that within the framework of the Cohen model we have definitely measured that r can be no greater than about 1.7. From Table I we see that Bate *et al.*[28] have measured $r \simeq 3$. Their measurements consisted of de Haas–Shubnikov-effect studies on tin-doped Bi. A doping level of 0.1 at.% was used to lower the Fermi energy into the L-point valence band, creating holes whose anisotropy was then measured. One implication of our result for r is that the doping level of tin used in Ref. 28 distorts the shape of the L-point valence band from the shape in pure Bi. In other words, the rigid-band model apparently does not hold for concentrations of tin in Bi of 0.1 at.%.

A feature of our results which offers strong evidence for the NENP model is the superior agreement between the hole and electron concentrations when the electron concentration is computed from the NENP model. The difference between n_+ and n_- is only 4% for the NENP mode, whereas the difference is 20% for the ENP model.

The QO results were consistent with both the ENP and NENP models, because of the lack of data at magnetic field orientations where differences are expected to exist. The standing-Alfvén wave results appear to be relatively insensitive to small distortions of the electron Fermi surface, since the period is an average over all pieces of the Fermi surface and small distortions are obliterated.

Our agreement with the NENP model is at odds with the results of the magnetoreflectance studies of Maltz and Dresselhaus[3] mentioned in the Introduction. The observation of the reflectance from a trigonal-plane sample as a function of magnetic field and incident photon energy is a fairly sensitive test to distinguish between the ENP and NENP models. Maltz and Dresselhaus find that a better fit is obtained with the ENP model. We are unable to offer a satisfactory explanation of this difference. It is possible that the NENP dispersion relation, although it approximates the constant-energy Fermi surface quite well, is not the proper description of the energy dispersion (i.e., the variation of surface shape with energy), and should be modified. However, there is no obvious way to modify the NENP dispersion relation to make the energy dispersion have the nonparabolic form of the ENP relation in the trigonal direction, yet retain the nonellipsoidal shape of the Fermi surface.

ACKNOWLEDGMENTS

It is a pleasure to acknowledge the advice and encouragement of Glen Everett. Conversations with Hans Churchill and the technical assistance of George Cooper have been invaluable.

APPENDIX

In this appendix we list the ENP and NENP electron-dispersion relations and cyclotron-mass anisotropies. The ENP dispersion relation is given by

$$E(1+\lambda) = \frac{P_1^2}{2m_1} + \frac{P_2^2}{2m_2} + \frac{P_3^2}{2m_3}, \tag{A1}$$

where $\lambda = E/E_g$, E_g is the valence-to-conduction-band energy gap, and the m_i are the effective-mass-tensor components at the bottom of the conduction band. The NENP dispersion relation is given by

$$E(1+\lambda) - \gamma \frac{P_2^2}{2m_2} - r \frac{P_2^4}{4m_2^2 E_g} = \frac{P_1^2}{2m_1} + \frac{P_3^2}{2m_3}, \tag{A2}$$

where $r = m_2/m_2'$, $\gamma = 1 + \lambda - \lambda r$, and m_2' is an effective-mass-tensor component at the top of the valence band.

The cyclotron effective mass for the NENP model is given by

$$m^*(\theta, \Omega) = \left(\frac{2m_1 m_2 m_3}{m_3 \cos^2\theta + m_1 \sin^2\theta} \right)^{1/2} \frac{1}{\pi b^{1/4} \cos\Omega} \times \left((1+2\lambda) K(k) + \frac{1-r}{r} \left[(\nu + \sqrt{b}) K(k) - 2(\sqrt{b})\, \epsilon(k) \right] \right), \tag{A3}$$

where

$$b = r\lambda(1+\lambda) + \nu^2,$$

$$\nu = \frac{m_2 \tan^2\Omega/\cos^2\theta + \gamma(m_3 + m_1 \tan^2\theta)}{2(m_3 + m_1 \tan^2\theta)},$$

$$k^2 = \frac{\sqrt{b} - \nu}{2\sqrt{b}},$$

and $K(k)$ and $\epsilon(k)$ are the complete elliptic integrals of the first and second kind, respectively. The angles θ and Ω define the direction of the applied magnetic field $\vec{H}$ with respect to the principal axes of the Fermi surface, as shown in Fig. 1 of I.

The ENP cyclotron-effective-mass anisotropy can be obtained from Eq. (A3) by setting $r = 1$, and taking $\nu^2 \gg r\lambda(1+\lambda)$.

*Work supported by the National Science Foundation.

†Present address: Physics Division, Michelson Laboratory, China Lake, Calif. 93555.

[1]R. Herrmann, S. Hess, and H. Mueller, Phys. Status Solidi B **48**, K151 (1971).

[2]M. H. Cohen, Phys. Rev. **121**, 387 (1961).

[3]M. Maltz and M. S. Dresselhaus, Phys. Rev. B **2**, 2877 (1970).

[4]B. Lax, Rev. Mod. Phys. **30**, 122 (1958); Bull. Am. Phys. Soc. **5**, 167 (1960).

[5]R. J. Dinger and A. W. Lawson, Phys. Rev. B **1**, 2418 (1970).

[6]R. J. Dinger and A. W. Lawson, Phys. Rev. B **3**, 253 (1971).

[7]V. S. Edel'man and M. S. Khaikin, Zh. Eksp. Teor. Fiz. **49**, 107 (1965) [Sov. Phys.-JETP **22**, 77 (1966)].

[8]Y. H. Kao, Phys. Rev. **129**, 1122 (1963).

[9]M. Ya. Azbel' and E. A. Kaner, Zh. Eksp. Teor. Fiz. **32**, 896 (1956) [Sov. Phys.-JETP **5**, 730 (1957)].

[10]L. Onsager, Philos. Mag. **43**, 1006 (1952).

[11]R. T. Isaacson and G. A. Williams, Phys. Rev. **177**, 738 (1969).

[12]R. T. Isaacson and G. A. Williams, Phys. Rev. **185**, 682 (1969).

[13]G. E. Everett, Phys. Rev. **128**, 2564 (1962).

[14]Further details of the experimental apparatus and technique can be found from R. J. Dinger, Ph.D. disseration (University of California, Riverside, 1971) (unpublished).

[15]G. S. Cooper and A. W. Lawson, Phys. Rev. B **4**, 3261 (1971). Also, see G. S. Cooper, Ph.D. dissertation (University of California, Riverside, 1970) (unpublished), for further details.

[16]E. H. Marston and Y. H. Kao, Phys. Rev. **182**, 504 (1969).

[17]D. S. McLachlan, Phys. Rev. **147**, 368 (1966).

[18]A. L. Jain, Phys. Rev. **114**, 1518 (1959).

[19]R. N. Brown, J. G. Mavroides, and B. Lax, Phys. Rev. **129**, 2055 (1963).

[20]D. Weiner, Phys. Rev. **125**, 1226 (1962).

[21]W. E. Engeler, Phys. Rev. **129**, 1509 (1963).

[22]L. C. Hebel and P. A. Wolff, Phys. Rev. Lett. **11**, 368 (1963).

[23]G. E. Smith, G. A. Baraff, and J. M. Rowell, Phys. Rev. **135**, A1118 (1964).

[24]D. M. Brown and S. J. Silverman, Phys. Rev. **136**, A290 (1964).

[25]L. Esaki and P. J. Stiles, Phys. Rev. Lett. **14**, 902 (1965).

[26]U. Strom, H. D. Drew, and J. F. Koch, Phys. Rev. Lett. **26**, 1110 (1971).

[27]N. B. Brandt, L. G. Lyubutina, and N. A. Kryukova, Zh. Eksp. Teor. Fiz. **53**, 134 (1967) [Sov. Phys.-JETP **26**, 93 (1968)].

[28]R. T. Bate, N. B. Einspruch, and P. J. May, Phys. Rev. **186**, 599 (1969).

[29]G. A. Antcliffe and R. T. Bate, Phys. Rev. **160**, 531 (1967).

[30]M. R. Ellet, R. B. Horst, L. R. Williams, and K. F. Cuff, J. Phys. Soc. Jap. Suppl. **21**, 666 (1966).

[31]M. S. Khaikin, R. T. Mina, and V. S. Edel'man, Zh. Eksp. Teor. Fiz. **43**, 2063 (1962) [Sov. Phys.-JETP **16**, 1495 (1963)].

[32]R. N. Bhargava, Phys. Rev. **156**, 785 (1967).

[33]S. Nagata and H. Kawamura, J. Phys. Soc. Jap. **24**, 480 (1968). A large number of typographical errors exist in their anisotropy equations.

[34]J. E. Aubrey, J. Phys. Chem. Solids **19**, 321 (1961).

[35]J. K. Galt, W. A. Yager, F. R. Merritt, B. B. Cetlin, and A. D. Brailsford, Phys. Rev. **114**, 1396 (1959).

[36]H. Kawamura, S. Nagata, T. Nakama, and S. Takano, Phys. Lett. **15**, 111 (1965).

[37]H. Kawamura, S. Nagata, S. Takano, and J. Nakahara, J. Phys. Soc. Jap. **21**, 734 (1966).

[38]N. B. Brandt and L. G. Lyubtina, Zh. Eksp. Teor. Fiz. **47**, 1711 (1964) [Sov. Phys.-JETP **20**, 1150 (1965)].

[39]J. E. Kunzler, F. S. L. Hsu, and S. W. Boyle, Phys. Rev. **128**, 1084 (1962).

[40]Y. Eckstein and J. B. Ketterson, Phys. Rev. **137**, A1777 (1965).

[41]R. D. Brown, Phys. Rev. B **2**, 928 (1970).